

**A high-resolution divergence and vorticity dataset in Beijing
derived from the radar wind profiler mesonet measurements**

Xiaoran Guo^a, Jianping Guo^a, Deli Meng^a, Yuping Sun^a, Zhen Zhang^{a,b}, Hui Xu^a,
Liping Zeng^c, Juan Chen^d, Ning Li^a, Tianmeng Chen^a

^a[State Key Laboratory of Severe Weather Meteorological Science and Technology](#),

Chinese Academy of Meteorological Sciences, Beijing 100081, China

^bDepartment of Atmospheric and Oceanic Sciences & Institute of Atmospheric
Sciences, Fudan University, Shanghai 200438, China

^cGuizhou New Meteorological Technology Co., Ltd, Guiyang 550001, China

^dAVIC Leihua Electronic Technology Research Institute, Wuxi 214063, China

Correspondence to:

[Dr./Prof. Jianping Guo](#) (Email: jpguocams@gmail.com)

Deleted: State

Deleted: Key Laboratory of Severe Weather

Deleted:

Abstract

Low-level convergence and cyclonic circulation are one of the most important dynamic variables in governing the initiation and development of convective storms. Our ability to obtain high-resolution horizontal divergence and vertical vorticity profiles, nevertheless, remains limited largely due to the lack of vertical wind observations. To fill this data gap, a high-density mesonet consisting of six radar wind profilers (RWP) sites has been operated in Beijing, which allowed for continuous observations of the three-dimensional winds with high vertical resolution. This paper aims to produce a temporally continuous horizontal divergence and vertical vorticity dataset at the vertical resolution of 120 m, which are derived from horizontal winds measured by the RWP mesonet in Beijing by using the triangle method. This dataset is generated at intervals of 6-minute for the whole year of 2023, covering the altitude range of 0–5 km. The dynamic variables from RWP mesonet are found to scatter sharply, as opposed to those from ERA5 that are concentrated around zero, especially at the high altitudes. Particularly, the negative divergence and positive vorticity are detected in the low-level troposphere up to 1 h in advance of the occurrence of rainfall events, and their magnitudes are increasingly becoming greater when the time comes closer to the rainfall onset, exhibiting the key role that the dataset plays in rainfall nowcasting. This is indicative of, to some extent, the effectiveness of high-resolution divergence and vorticity dataset in Beijing. The dataset is publicly available at <https://doi.org/10.5281/zenodo.15297246> (Guo and Guo, 2024a), which is of significance for a multitude of scientific research and applications, including convection initiation, air quality forecasting, among others. Therefore, the findings highlight the urgent need of exploiting the dynamic variables from the RWP mesonet measurements to better characterize the pre-storm environment.

Deleted: 07

Deleted: <https://doi.org/10.5281/zenodo.14176969>

Deleted: et al.

Short Summary

Optimal atmospheric dynamic condition is essential for convective storms. This study generates a dataset of high-resolution divergence and vorticity profiles using the measurements of radar wind profiler mesonet in Beijing. The negative divergence and positive vorticity are present in advance of rainfall events. This suggests that this dataset can help improve our understanding of pre-storm environment and has the potential to be applied to weather forecasting.

1. Introduction

Atmospheric dynamic conditions, such as vorticity, divergence, and vertical velocity, play a critical role in inferring convection initiation (CI) and the subsequent development of mesoscale convective systems (MCSs) (Ulanski and Garstang, 1978; Weckwerth and Parsons 2006; Wilson and Roberts 2006; Lock and Houston 2014; Weckwerth et al., 2019; Guo et al., 2024b). In recent decades, a variety of previous observational analysis based on passive surface stations and weather radars reveal the positive correlation between surface convergence and the formation of new convective cells (Purdom 1976; Fankhauser et al., 1995; Kalthoff et al., 2009; Bai et al., 2019). The sustained and enhanced updraft forced by local convergence is conducive to the initiation or intensification of convective cells, especially in unstable and deep moist environments. Furthermore, the interaction between wind shear and vertical vorticity structure produces favorable atmospheric conditions for cyclogenesis in both midlatitude and tropical regions during the warm season (Bosart and Sanders, 1981; Zhang and Fritsch, 1987). The pressure drop caused by the cyclonic rotation of the low-level mesocyclone further accelerates the lifting, as described by the mesoscale vertical vorticity equation used in vertical velocity analyses (Yanai and Nitta, 1967; Brandes and Ziegler, 1993, Shapiro et al., 2009).

84 Additionally, the radiosonde sounding arrays have been used to obtain the
85 vertical wind profiles that are further applied for retrievals of atmospheric dynamic
86 variables over large spatial scales exceeding 500 km. In this case, the wind gradients
87 are objectively determined by the linear interpolation to grid points using observations
88 of distant stations with inevitable errors (Lee and Browning, 1993). Afterwards, many
89 follow-on studies confirmed its possibility to realistically calculate the mass
90 divergence of the air over an area by using soundings or dropsondes distributed along
91 the perimeter of this area (e.g., Holland and Rasmusson, 1973; Nitta and Esbensen,
92 1974; Lenschow et al., 1999, 2017). On the other hand, vertical vorticity can be
93 directly determined from Stokes theorem using closed integrals of the horizontal
94 velocity tangent component enclosing the area. For instance, Davies-Jones (1993)
95 investigated the algorithms to estimate vertical vorticity profiles and associated errors
96 over sub-synoptic scale regions from a small number of observing stations. During an
97 airborne field campaign over the tropical Atlantic near Barbados, the dropsondes with
98 horizontal wind profile measurements were released with high frequency along
99 circular flight patterns to estimate vertical profiles of the area-averaged mass
100 divergence and vorticity (Bony and Stevens, 2019). Nevertheless, it is proved that the
101 triangle method is more practical in operation if observations are irregularly
102 distributed (Bellamy, 1949).

Deleted: calcualte

103 Nowadays, divergence and vorticity over smaller areas, with linear dimensions on
104 the order of 100 km, have attracted widespread attention due to the importance of
105 mesoscale vertical motions (Bony et al., 2017). With the advent of dense remote
106 sensing instruments, more accurate retrievals of divergence and vorticity profiles are
107 more possible due to wind fields with higher precision and resolution. A new
108 generation of ground-based radar wind profiler (RWP) network has been operated in
109 China as of 2008 (Guo et al., 2021a), which consists of over 260 stations by the end of
110 2023. It has good spatial coverage with six RWP sites over Beijing, which provide
111 continuous observations of high-resolution three-dimensional wind fields (Liu et al.,
112 2019; Guo et al., 2023). In our previous study (e.g., Guo et al, 2023, 2024b; Chen et

Deleted: the

Deleted: metropolitan region (BMR)

al., 2024), the vertically resolved dynamic parameters were calculated from the measurements of RWP mesonet to identify the pre-storm conditions and forecast the ensuing evolution of MCSs.

In the present study, a long-term horizontal divergence and vertical vorticity datasets covering the whole year of 2023 are generated, which have crucial implications for the identification and evaluation of vertical motion and convection development. The rest of the paper is organized as follows. Section 2 describes the fundamental data sets and the calculation methodology used here. A comparison analysis is conducted of dynamic variable profiles between RWPs retrieval and ERA5 reanalysis in Section 3. Sections 4 represented the variation patterns of these two dynamic parameters preceding rainfall events. Main conclusions are given in the final section.

2. Data and Methodology

2.1 Radar wind profiler measurements

Figure 1 presents the RWPs mesonet deployed in Beijing at the following stations: Huairou (HR; 40.36°N, 116.63°E), Yanqing (YQ; 40.45°N, 115.97°E), Shangdianzi (SDZ; 40.66°N, 117.11°E), Pinggu (PG; 40.17°N, 117.12°E), Haidian (HD; 39.98°N, 116.28°E), and the Beijing Weather Observatory (BWO). These RWPs are Ce Feng Leida-6 (CFL-6) Tropospheric Wind Profilers, which are produced by the 23rd Institute of China Aerospace Science and Industry Corporation (Table 1). They provide measurements of horizontal and vertical winds, and refractive index structure parameter at 6-min intervals. The vertical resolution is 120 m from 0.15 to 4.11 km above the ground level (AGL) in low-operating mode, and 240 m from 4.11 to 10.11 km AGL in high-operating mode (Liu et al., 2019).

The RWPs detect vertically resolved wind fields by transmitting and receiving electromagnetic beams in five directions, including a zenith and four inclined directions of 15° in the east, south, west and north, respectively. By analyzing the

Formatted: Font: 12 pt, Not Bold

Formatted: Level 2, Space Before: 0 pt, After: 0 pt, Line spacing: 1.5 lines

Deleted: 2.1 Radar wind profiler measurements

Deleted: the BMR's RWP mesonet, which consists of six

Formatted: Font: (Asian) DengXian

Formatted: Font: (Asian) DengXian

Formatted: Font: (Asian) DengXian

Formatted: Font: (Asian) DengXian

Formatted: Font: (Asian) DengXian

Formatted: Font: (Asian) DengXian

Formatted: Font: (Asian) DengXian

Formatted: Font: (Asian) DengXian

Formatted: Font: (Asian) DengXian

Formatted: Font: (Asian) DengXian

Formatted: Font: (Asian) DengXian

Formatted: Font: (Asian) DengXian

Formatted: Font: (Asian) DengXian

Formatted: Font: (Asian) DengXian

Formatted: Font: (Asian) DengXian

Formatted: Font: (Asian) DengXian

Formatted: Font: (Asian) DengXian

Formatted: Font: (Asian) DengXian

Formatted: Font: (Asian) DengXian

Formatted: Font: (Asian) DengXian

Formatted: Superscript

Deleted: RWP

Deleted: mesonet

Deleted: s

Deleted: below 4 km

Doppler shifts of radial velocities from any three beams, horizontal and vertical wind components are retrieved. However, the falling of small targets (particulate scatterers) and raindrops may cause the potential biases of vertical velocity in such a way that vertical velocity cannot usually be used directly (Angevine, 1996; Wang et al., 2014; McCaffrey et al., 2017). The fluctuating component of the horizontal velocity is not affected under varying meteorological conditions since it is much larger in magnitude.

To ensure the integrity of the data, a test for the acquisition rate of the horizontal wind profiles spanning a whole year of 2023 is conducted. As shown in Figure 1b, the observations below 4.11 km AGL for six RWP's relatively meet the requirements of continuity in time with the average missing rate less than 20%. These relatively low acquisition of the RWP data at high altitude could be attributed to the well-known limitations that the radar signal attenuation constitutes the inherent uncertainty sources. Therefore, the horizontal winds derived from six RWP's at the heights of 0.15–4.11 km AGL in 2023 are collected in this study.

2.2 Evaluation of horizontal winds of RWP

To further evaluate the data quality of the RWP's, horizontal wind speeds at every level from the BWO are validated against the coincident radiosonde measurements. Upper-air sounding balloons are launched at the BWO twice daily at 0800, and 2000 Local Standard Time (LST), providing the vertical profiles of temperature, pressure, relative humidity, and horizontal winds with a vertical resolution of 5–8 m (Guo et al., 2021b). During summer months (June-July-August), an intensive observation campaign has been conducted at most radiosonde stations of China with an additional balloon launches at 1400 LST. As shown in Figure 1c, the correlation coefficient (R) is found greater than 0.8 from 0.51 to 4.11 km AGL. Nevertheless, the accuracy and reliability of the RWP data below 0.51 km is limited by the interference of near-surface clutter. Scatterplots obtained by aggregating all the samples between 0.51 and 4.11 km AGL produce a correlation coefficient (R) value as high as 0.84 (Figure 1d). Thus, the horizontal winds derived from RWP's in the

Formatted: Level 2, Indent: First line: 0 cm, Space Before: 0 pt, After: 0 pt, No widow/orphan control, Keep with next, Keep lines together

Formatted: Font: (Asian) DengXian Light, Italic

Deleted: 0

Deleted: is added

Deleted: From

Deleted: was

Formatted: Not Highlight

Formatted: Not Highlight

Deleted: According to the validation results against radiosonde measurements in BWO by Guo et al. (2023), the

heights of 0.51–4.11km AGL are believed to be reliable enough and then be adopted here for the generation of atmospheric dynamic dataset.

2.3 Rain Gauge Measurements and reanalysis

Rainfall at 1-min interval is directly acquired from the rain gauge measurements at automated surface stations over Beijing. Here, 6-min accumulated rainfall is synchronized with the RWP measurements at 6-min interval. These rain gauge measurements have undergone rigorous quality control and are publicly available by the China Meteorological Administration.

ERA5 is the fifth-generation atmospheric reanalysis of ECMWF (European Centre for Medium-Range Weather Forecasts), which benefits from advancements in data assimilation, model physics and dynamics (Hersbach et al., 2020). ERA5 dataset can provide divergence and vorticity on 37 pressure level with a spatial resolution of $0.25^\circ \times 0.25^\circ$ at hourly intervals. Additionally, the planetary boundary layer (PBL) height product is directly obtained from the ERA5 reanalysis.

2.4 Calculation of horizontal divergence and vertical vorticity

Generally, the horizontal divergence D and vertical vorticity ζ are represented by pairs of partial derivatives of velocity to reflect the change of air velocities with distance. By applying the Gauss's theorem, horizontal divergence D is expressed by the relative expansion rate of the air mass. The triangle method, as proposed by Bellamy (1949), computes the divergence based on the rate of change in a fluid triangle initially coincident with the network composed by any three points A , B , and C . We assume that $(x_i, y_i) (i = A, B, C)$ are the location of three vortex points, $\vec{V}_i = (u_i, v_i)$ are the zonal and meridional component of horizontal wind, respectively. As the air parcel at (x_i, y_i) moves to $(x_i + u_i \Delta t, y_i + v_i \Delta t)$ after the infinitesimally short time Δt , a new triangle $A'B'C'$ will form. The resultant horizontal divergence D over the fluid triangle can be defined as

Deleted: altitude rang

Formatted: Not Highlight

Deleted: e

Formatted: Not Highlight

Deleted: 5km

Deleted:)

Formatted: Not Highlight

Deleted: above the ground level (

Deleted: spanning a whole year of 2023

Deleted: ¶

Deleted: 2

Formatted: Indent: First line: 0 ch, Widow/Orphan control

Field Code Changed

Field Code Changed

Deleted: (

$$D = \frac{1}{\sigma} \frac{d\sigma}{dt} = \frac{1}{\sigma} \lim_{\Delta t \rightarrow 0} \frac{\Delta\sigma}{\Delta t} = \frac{1}{\sigma} \lim_{\Delta t \rightarrow 0} \frac{\sigma' - \sigma}{\Delta t} \quad (1)$$

where σ and σ' denote the area of the triangle ABC and $A'B'C'$, which can be formulated by

$$\sigma = \frac{1}{2} (\overrightarrow{AB} \times \overrightarrow{AC}) \cdot \vec{k} = \frac{1}{2} \begin{vmatrix} \vec{i} & \vec{j} & \vec{k} \\ x_B - x_A & y_B - y_A & 0 \\ x_C - x_A & y_C - y_A & 0 \end{vmatrix} \cdot \vec{k} \quad (2)$$

$$\sigma' = \frac{1}{2} (\overrightarrow{A'B'} \times \overrightarrow{A'C'}) \cdot \vec{k} = \frac{1}{2} \begin{vmatrix} \vec{i} & \vec{j} & \vec{k} \\ (x_B + u_B \Delta t) - (x_A + u_A \Delta t) & (y_B + v_B \Delta t) - (y_A + v_A \Delta t) & 0 \\ (x_C + u_C \Delta t) - (x_A + u_A \Delta t) & (y_C + v_C \Delta t) - (y_A + v_A \Delta t) & 0 \end{vmatrix} \cdot \vec{k} \quad (3)$$

Here, \vec{i} , \vec{j} , \vec{k} represent the unit vectors of zonal, meridional and the vertical axis in the coordinate system, respectively. Substituting Eqs. (3) and (2) into Eq. (1) and

simplifying, the triangle-area averaged horizontal divergence is as follows

$$D = \frac{(u_B - u_A)(y_C - y_A) - (u_C - u_A)(y_B - y_A) + (x_B - x_A)(v_C - v_A) - (x_C - x_A)(v_B - v_A)}{(x_B - x_A)(y_C - y_A) - (x_C - x_A)(y_B - y_A)} \quad (4)$$

The vertical vorticity ζ can be estimated directly from Stokes theorem as

$$\zeta = \frac{1}{\sigma} \oint \vec{V} \cdot d\vec{r} \quad (5)$$

Circulation along the triangle ABC can be calculated by

$$\oint \vec{V} \cdot d\vec{r} = \frac{(\vec{V}_A + \vec{V}_B) \cdot \overrightarrow{AB}}{2} + \frac{(\vec{V}_B + \vec{V}_C) \cdot \overrightarrow{BC}}{2} + \frac{(\vec{V}_C + \vec{V}_A) \cdot \overrightarrow{CA}}{2} \quad (6)$$

Substituting Eqs. (2) and (6) into Eq. (5), the vertical vorticity is as follows

$$\zeta = \frac{(v_B - v_A)(y_C - y_A) - (v_C - v_A)(y_B - y_A) - (x_B - x_A)(u_C - u_A) + (x_C - x_A)(u_B - u_A)}{(x_B - x_A)(y_C - y_A) - (x_C - x_A)(y_B - y_A)} \quad (7)$$

These equations are then applied to the above-mentioned wind measurements from the RWP mesonet in order to calculate the profile of horizontal divergence and vertical vorticity. Four triangles from west to east are constructed based on the

Formatted: Centred

Deleted:

Field Code Changed

Deleted:

Deleted:

Deleted:

Formatted: Centred

Field Code Changed

Formatted: Left

Field Code Changed

Deleted:

Deleted:

Formatted: Font: DengXian, 10,5 pt, Font colour: Auto

Formatted: Right

Field Code Changed

Deleted: ¶

Field Code Changed

Deleted:

Deleted:

Deleted: <object>

Formatted: Right: 1,48 cm, Allow text to wrap in the middle of a word

Formatted: Font: Times New Roman, 11 pt

Deleted: ¶

Formatted: Centred

$$\oint \vec{V} \cdot d\vec{r} = \frac{(\vec{V}_1 + \vec{V}_2) \cdot \overrightarrow{AB}}{2} + \frac{(\vec{V}_2 + \vec{V}_3) \cdot \overrightarrow{BC}}{2} + \frac{(\vec{V}_3 + \vec{V}_1) \cdot \overrightarrow{CA}}{2}$$

Deleted:

Deleted:

Deleted:

Deleted: where is the vector of the horizontal wind at . ¶

Formatted: Centred

Deleted:

Deleted:

positions of RWP stations in Beijing. It is noteworthy that the denominator of Eqs. (4) and (7) is equal to the area of triangle from Eq (2). That's to say, the value of divergence and vorticity is inversely proportional to the area of triangle. Therefore, the magnitudes of results are larger for triangle 2, which could be attributed partly to the smallest area of triangle 2 used for area-averaged calculations compared to those of other triangles. This coincides with the fact that the gradient of velocity between two points, including $\frac{\partial u}{\partial x}$, $\frac{\partial v}{\partial x}$, $\frac{\partial u}{\partial y}$ and $\frac{\partial v}{\partial y}$, will increase when the distance is shortened. Considering the six RWPs located at different terrain elevations, the horizontal velocities measured by each RWP are interpolated to the same altitude that starts upwards from 0.51 km to 4.95 km above mean sea level (AMSL) with a vertical resolution of 120 m.

3. Comparison analysis of dynamic variables from RWP with those from ERA5

Due to the widespread usage of ERA5 reanalysis in characterizing stable condition of atmosphere, evaluating its performance in representing the vertical profiles becomes crucial. The divergence and vorticity fields derived from the RWP mesonet are compared with ERA5 reanalysis in the non-precipitation day in this section. To match the spatial resolution of the ERA5 dataset on the grid of $0.25^\circ \times 0.25^\circ$ to the RWP mesonet, divergence and vorticity profiles of all the grids within this triangle are averaged for each triangle. Simultaneously, observed profiles at 1-hour interval are applied in accordance with the temporal resolution of reanalysis.

It is well known that the PBL is the lowermost part of the troposphere that governs the exchange of momentum, mass and heat between surface and atmosphere (Adler et al., 2014; Dai et al., 2014; Dodson and Griswold, 2021; Su et al., 2023). Considering that the altitude z is used in this study instead of height above ground level, z_i for a given triangle equals to the terrain height plus and PBL height. To better reveal how the divergence and vorticity vary with PBL, z can be normalized by z_i to

Deleted: the BMR

Formatted: Font: Times New Roman, 12 pt

Deleted: 2.3 Rain Gauge Measurements and ERA5 reanalysis ¶

Rainfall at 1-min interval is directly acquired from the rain gauge measurements at automated surface stations over Beijing. Here, 6-min accumulated rainfall is synchronized with the RWP measurements at 6-min interval. These rain gauge measurements have undergone rigorous quality control and are publicly available by the China Meteorological Administration. ¶

ERA5 is the fifth-generation atmospheric reanalysis of ECMWF (European Centre for Medium-Range Weather Forecasts), which benefits from advancements in data assimilation, model physics and dynamics (Hersbach et al., 2020). ERA5 dataset can provide divergence and vorticity on 37 pressure level with a spatial resolution of $0.25^\circ \times 0.25^\circ$ at hourly intervals. Additionally, the planetary boundary layer (PBL) height product is directly obtained from the ERA5 reanalysis. ¶

Deleted: ¶

Formatted: Not Highlight

Deleted: There are significant differences between the wind field in the PBL and the upper atmosphere. , an important parameter z_i is defined To to better reveal the characteristics of divergence and vorticity at different heights. Normally, the PBL height stands for the distance from the top of PBL to the Earth's surface. ,

Deleted: ,

Deleted: each

Deleted: consists of two

Deleted: parts:

Deleted: average

Deleted: of that triangle

Deleted: the average

Deleted: above

Deleted: The altitude

Deleted:

Formatted: Font: Italic

Formatted: Not Highlight

provide a nondimensional vertical coordinate for horizontal divergence and vertical vorticity in the following analyses. The layers at the range of 0.51–4.11 km AMSL is classified as near-surface, low-level, and mid-level layer according to the criterion of $z/z_i \leq 1$, $1 < z/z_i \leq 2$, $z/z_i > 2$, respectively. Figure 2 shows the normal distribution of the two dynamic parameters derived from RWP mesonet and ERA5 reanalysis for all non-precipitation day in 2023. Overall, the distributions of observed parameters on the different altitude layer are similar. The value of divergence and vorticity by ERA5 reanalysis are more significantly concentrated in zero, indicating that the ERA5 reanalysis underestimates the amplitude compared with the RWP mesonet measurements. The higher peak probability is found in the low-level and mid-level troposphere. This illustrates that ERA5 reanalysis does not detect well divergence and vorticity at higher altitudes, which resembles the results in previous studies (Taszarek et al., 2021; Wu et al., 2024). We speculate the difference may be likely resulted from insufficient wind profiling measurements in China being assimilated into ERA models.

To further explore the overall differences of vertical profiles between reanalysis datasets and observation more quantitatively, divergence and vorticity from RWP mesonet measurements are validated against ERA5 after interpolating the reanalysis to corresponding level. As shown in Figure 3a-c, ERA5 reanalysis cannot characterize the potential horizontal and vertical motion in a non-precipitation environment with the correlation coefficient (R) less than 0.1. It's also evident that ERA5 exhibits a substantial underestimation of divergence, especially at the higher altitudes. Noteworthy is that ERA5 reanalysis exhibits better performance in representing vertical vorticity with R reaching 0.3 even though the disparity is still apparent (Figure 3d-f). This could be due to the magnitude of vorticity being greater than that of divergence.

Deleted: for

Formatted: Not Highlight

Deleted: the sum of the average elevation and PBL height are defined as z_i

Formatted: Not Highlight

Deleted: altitude

Formatted: Not Highlight

Deleted: -

Formatted: Not Superscript/ Subscript

Deleted: normalized by z_i to provide a nondimensional vertical coordinate for horizontal divergence and vertical vorticity. The criterion of z/z_i is set as 1 and 2 to separate separate different altitude layers to near-surface, low-level, and midlevel layer for the following analyses. Fig

Deleted:

Deleted: separate different altitude layers to near-surface, and midlevel layer for the following analyses. Fig

4. Height-resolved dynamic conditions preceding rainfall events

4.1 Statistical characteristics of the two dynamic variables

The ERA5 reanalysis with lower temporal resolution is recognized to have limited capability of characterizing the temporally continuous evolution of atmospheric motion in a pre-storm environment over a mesoscale region. It is desirable to fill this gap with height-resolved dynamic variables as calculated with the RWP mesonet measurements at 6-min intervals. In this section, we attempt to explore how the horizontal divergence and vertical vorticity derived from the RWP mesonet could be used as precursors for the pre-storm environment conditions. The triangle-area-averaged 6-min rainfall amount (mm), which is obtained from 29, 42, 49, and 15 rain gauges in triangles 1, 2, 3, and 4 respectively, is used to identify rainfall events occurring during the whole year of 2023 over the Beijing's RWP mesonet. For each triangle, all rainfall moments are selected when the 6 min accumulated triangle-area-averaged rainfall is greater than zero. Considering the intermittent nature of rainfall, all the adjacent rainfall events being separated by less than 2 hours are classified as the same rainfall event. That's to say, the interval between two rainfall events is required to be at least 2 hours. The first and last rainfall moment of every rainfall event are defined as the occurrence and ending time of rainfall event, respectively. To avoid the impact of data error, the rainfall events with duration of less than 30 minutes are discarded. Finally, a total of 462 rainfall events are identified over the RWP mesonet in 2023.

Figure 4a and 4b present the normalized contoured frequency by altitude (NCFAD) for all profiles of the horizontal divergence and vertical vorticity as observed by the RWP mesonet in non-precipitation days, respectively. Specifically, the values of horizontal divergence and vertical vorticity are overall distributed around zero above 2.5 km AMSL. The magnitude of vorticity is greater than that of divergence with more vertical fluctuation in the mid-troposphere. Weak diffluence as indicated by positive divergence values exists in the lower troposphere below 2 km AMSL. By comparison, the pre-storm dynamic environment within 1-hour preceding

Deleted: temporal patterns of

Deleted: variables

Deleted: the onset of

Formatted: Level 2, Space Before: 0 pt, After: 0 pt, Line spacing: 1,5 lines

Formatted: Font: (Asian) DengXian Light, 12 pt, Not Bold, Italic

Deleted: BMR

Deleted: within 1-hour preceding rainfall events

Deleted: The

rainfall events (Figure 4c and 4d) exhibits significant difference, which implies the presence of complex vertical motion in this unstable atmosphere. The divergence below 1 km AMSL significantly concentrates from $-5 \times 10^{-5} \text{ s}^{-1}$ to zero before rainfall events (Figure 4c). As indicated in Figure 4d, the lowest layer is dominated by positive vorticity centering near 1 km AMSL.

By using dynamic parameters with higher temporal resolution obtained from the RWP mesonet, our aim is to further explore potential patterns or trends in the pre-rainfall convection environment during the lead time. Figures 5a and 5b show the evolutions of average profiles of horizontal divergence and vertical vorticity at 12-min interval before the occurrence of rainfall events. The significant increase in average convergence below 1.5 km AMSL within 48 min ahead of precipitation (Figure 5a) is largely contributed to the fact that near-surface air tends to strongly converge into the pre-squall mesotrough when convective system approaches. The main convection was collocated with low-level convergence and mid-level divergence placed ahead of the precipitation center. These patterns are consistent with previous studies (Wilson and Schreiber, 1986; Zhang et al., 1989; Qin and Chen, 2017; Yin et al., 2020).

Similarly, the increase in vertical vorticity shown in Figure 5b might be associated with significant horizontal wind shear. The preexisting ambient wind field before the arrival of MCS is critical to system organization since the orientation of its vertical shear directly influences an asymmetric precipitation structure with mesoscale rotation. In addition, the mesoscale convectively vortex (MCV) may be resulted from deep and moist convection prior to the passage of the MCS (Wang et al. 1993). Trier et al. (1997) indicated that the MCS-induced horizontal flow and its associated vertical shear are critical factors which influence the development of the vortex. This southwesterly flow, enhanced by the MCV circulation, transports moisture northward in the lower troposphere, thereby creating potential instability ahead of the vortex center. Such an environment is favorable for convection and further lead heavy precipitation (Johnson et al., 1989; Hendricks et al., 2004; Lai et al., 2011).

Formatted: Font: Times New Roman, 12 pt

Formatted: Indent: First line: 2 ch

Deleted: ¶

Specifically, the horizontal divergence with maximum frequency appears about 0 above 1 km AMSL (Figure 4a). In contrast, the divergence below 1 km AMSL significantly concentrates from $-5 \times 10^{-5} \text{ s}^{-1}$ to 0. The presence of weak convergence, as indicated by negative value of divergence, is possibly associated with topography. In spite of this weaknesses, convergence tends to provide favorable upward motions in the lower troposphere. These upward motions represent the important lifting of moist air near surface that facilitates the subsequent formation of clouds and onset the convective rainfall. Typically, Wilson and Schreiber (1986) extensively elucidated the potential precursors of convergent processes in the PBL to CI and intensifying existing storms by providing locally enhanced updrafts. ...

Deleted: the

Deleted: As indicated in Figure 4b, the magnitude of vorticity is greater than that of divergence with more vertical fluctuation in the lower to mid-troposphere. The lowest layer is dominated by positive vorticity centering near 1 km

Deleted: significant

Deleted: be in part attributed to the preexisting ambient vorticity associated with significant horizontal wind shear. ...

Formatted: Not Highlight

Deleted: environmental

Deleted: by the

4.2 Temporal patterns of divergence during a convective process

Due to the direct connection between horizontal divergence and vertical motion, we attempt to further discuss how the RWP-derived divergence could practically benefit short-term forecasting of a convective rainfall event. The evolution of 30-min accumulated rainfall from rain gauge measurements is given in Figure 6. After 0400 LST 22 July, 2023, an early-morning event occurred in Beijing with a maximum rainfall rate exceeding 10 mm within 30 minutes. This event was associated with the transport of moisture as the subtropical moved northward. The main region of precipitation was located to the southeast of Beijing before 0500 LST, there was no significant rainfall within the RWP mesonet (Figure 6a, b). As the major convective storm slowly propagated northward and approached the edge of triangle 3 after 0500 LST (Figure 6c), the precipitation then took place. Interestingly, a few new cells at the meso- γ -scale formed in triangle 1 at the same time (Figure 6d-e) and expanded rapidly to other triangles (Figure 6f-h). The uneven precipitation caused by these isolated and scattered convection cells was a difficult problem in monitoring and nowcasting. Of relevance to this study was the potential application of the RWP-derived divergence profiles for capture the CI and subsequent rainfall.

Figure 7a–d display the time series of the rainfall rates and vertical profiles of the area-averaged divergence during the period of 0400–0730 LST 22 July, 2023 in triangles 1–4 respectively. Specifically, one can see the presence of weak convergence below 2 km AMSL with significant divergence above after 0400 LST in triangle 1 (Figure 7a). Subsequently, the convergence layer deepened up to 3.5 km AGL from 0430 LST. The low-level convergence simultaneously strengthened with the maximum value of $-1.4 \times 10^{-4} \text{ s}^{-1}$ near 1 km AMSL at 0448 LST. The signals of prevailing convergence in the lower troposphere provided favorable upward motions for the important lifting of water vapor in the PBL in advance of the convective rainfall. The more intense convergence and upward motion were also well detected in triangle 2 below 1.23 km AMSL after 0448 LST (Figure 7b), which coincided with the generation of rainfall in triangle 1. The inflow over triangle 2 could be attributed

Formatted: Font: (Default) Times New Roman

Formatted: Not Highlight

Deleted: from

Formatted: Not Highlight

Formatted: Not Highlight

Formatted: Not Highlight

Formatted: Superscript

Formatted: Superscript, Not Highlight

Formatted: Superscript

Formatted: Superscript

to the fact that cold downdraft air in triangle 1 tended to converge into the mesotrough ahead of convection. Even considering the strongest convergence of triangle 2 was resulted from the smallest area to a certain extent, such a significant enhanced trend was evident. Similarly, the rainfall in triangle 2 started at 0530 LST closely related to pronounced convergence and upward motion in the lower troposphere.

As shown in Figure 7c and 7d, the relationship between vertical profiles of divergence and rainfall for triangle 3 and 4 during the rainy period was analogous to that for triangle 1 and 2. Nevertheless, triangle 3 and 4 experienced relatively weaker low-level convergence below 1.5 km AMSL. The presence of dominated divergence layer above is not conducive to the extension of upward movement and formation of convective clouds. The weaker peak area-averaged rainfall rate was seen in triangle 3 and 4 in contrast. Clearly, it has been proved that the RWP mesonet has the capability of detecting the continuous vertical profiles of divergence leading to the onset of precipitation at high spatial and temporal resolutions. However, the development of convection is also affected by many other thermal and dynamic variables, it should be noted that it's feasible to qualitatively determine the change of rainfall rather than quantitatively.

5. Concluding remarks and summary

The generation and organization of convergence and rotation are the recurring theme of baroclinic convection in midlatitude during the warm season. Owing to relatively few direct observations, the detailed structure of MCSs has not been exactly explored. The unique aspect of this study is the analysis of the enhanced observations derived from the new-generation ground-based RWP mesonet in Beijing. The RWP mesonet is shown being capable of continuously observing the horizontal wind fields in the lower troposphere with ultra-high vertical and temporal resolutions. The horizontal wind measurements are then used to calculate the vertical profiles of the triangle-area-averaged horizontal divergence and vertical vorticity, which is well indicative of the dynamic structure in the lower to mid-troposphere.

Deleted: ¶

505 Compared to the vertical profiles with higher accuracy, ERA5 exhibits a
506 substantial underestimation of divergence and vorticity, especially at the higher
507 altitudes. ERA5 reanalysis cannot characterize the potential horizontal and vertical
508 motion even in a non-precipitation environment. The limitation may be likely due to
509 the lack of higher-level wind profiling measurements in China being assimilated into
510 ERA models. In addition, ERA5 reanalysis is unable to identify the propagation of
511 MCSs and provide the real-time precursor signals of precipitation. The RWP-derived
512 convergence and cyclonic circulation can provide useful information with a temporal
513 resolution of 6-minute for detecting rainfall initiation, and filling the gap of sounding
514 and reanalysis for nowcasting the occurrence of rainfall events.

Deleted: , which

515 For this purpose, a statistical analysis of the vertical divergence and vorticity
516 profiles preceding rainfall events over the RWP mesonet in 2023 are performed.
517 Results show that the patterns of increasing low-level convergence and cyclonic
518 circulation is evident before the occurrence of rainfall events. This indicates the
519 development of the corresponding upward motion, at least in the lower troposphere,
520 prior to the arrival the passage of the storm, respectively. The convergence near the
521 surface, in combination with the low-level cyclonic rotation, provide favorable
522 dynamic conditions to lift moist air for the subsequent formation of clouds and onset
523 the convective rainfall.

524 In conclusion, the RWP mesonet can be used to calculate the vertical profiles of
525 divergence and vorticity in the lower to mid-troposphere more realistically compared
526 to reanalysis dataset. These dynamic variables from observations can provide useful
527 information for characterizing the process of convection and detecting rainfall
528 initiation in advance. It is imperative to apply them to nowcasting of severe weather
529 events as well as the improvement of initial conditions in numerical weather
530 prediction models. While the results presented above are encouraging, the potential
531 effects of the heterogeneous urban landscape and complex terrain of the Beijing
532 region cannot be discussed temporarily. Furthermore, the observational gaps near
533 surface need to be filled by wind lidars in a forthcoming study, which will be

Deleted: it is imperative to

Deleted: the observational gaps near surface

beneficial for exploring the bifurcation of flow by the high risings over the built-up area and revealing the mesoscale circulation by the urban heat island effect.

Deleted: and apply them to nowcasting of severe weather events as well as the improvement of initial conditions in numerical weather prediction models. Furthermore, the orographic influence on the structure of the convergence, vortex and precipitation will also be explored in a forthcoming study....

Author contributions

JG designed the research framework and conceptualized this study; XG and JG conducted the experiment and drafted the initial manuscript; TC and NL helped the data collection and carried out the quality control. LZ, JC, FZ and YS contributed to the revision of the manuscript. All authors participated in result interpretation.

Competing interests

The contact author has declared that there are no competing interests for all authors.

Financial support

This manuscript was jointly under the auspices of the National Natural Science Foundation of China under grants of 42325501, the Chinese Academy of Meteorological Sciences under grant 2024Z003 and the Department of Science and Technology of Guizhou province under grant KXJZ [2024] 033.

Data availability

The divergence and vorticity dataset over Beijing can be accessed at <https://doi.org/10.5281/zenodo.15297246>, (Guo and Guo, 2024a). We are grateful to ECMWF for providing ERA5 hourly data, which are available at <https://www.ecmwf.int/en/forecasts/datasets/reanalysis-datasets/era5/>. The meteorological measurements of automatic weather stations are obtained from the National Meteorological Information Center of China Meteorological Administration (<https://data.cma.cn>) via registration.

Deleted: <https://doi.org/10.5281/zenodo.14176969>

Deleted: et al.

References

- Adler, B. and Kalthoff, N.: Multi-scale transport processes observed in the boundary layer over a mountainous island, *Bound.-Lay. Meteorol.*, 153, 515 – 537, <https://doi.org/10.1007/s10546-014-9957-8>, 2014.
- Angevine, W. M.: Errors in mean vertical velocities measured by boundary layer wind profilers, *Journal of Atmospheric and Oceanic Technology*, 14, 565, doi: 10.1175/1520-0426(1997)0142.0.CO;2, 1996.
- Bai, L., Meng, Z., Huang, Y., Zhang, Y., Niu, S., and Su, T.: Convection initiation resulting from the interaction between a quasi-stationary dryline and intersecting gust fronts: A case study, *Journal of Geophysical Research: Atmospheres*, 124, 2379–2396. <https://doi.org/10.1029/2018JD029832>, 2019.
- Bellamy, J.C.: Objective calculations of divergence, vertical velocity and vorticity, *Bull. Amer. Meteor. Soc.*, 30, 45–49, <https://doi.org/10.1175/1520-0477-30.2.45>, 1949.
- Bony, S., Stevens, B., Ament, F., and Coauthors: EUREC⁴A: A field campaign to elucidate the couplings between clouds, convection and circulation, *Surv. Geophys.*, 38, 1529–1568, <https://doi.org/10.1007/s10712-017-9428-0>, 2017.
- Bony, S., and Stevens, B.: Measuring area-averaged vertical motions with dropsondes, *J. Atmos. Sci.*, 76, 767–783, <https://doi.org/10.1175/JAS-D-18-0141.1>, 2019.
- Bosart, L. F., and Sanders, F.: The Johnstown flood of July 1977: A long-lived convective storm, *J. Atmos. Sci.*, 38(8), 1616 – 1642, doi: 10.1175/1520-0469(1981)038<1616:TJFOJA>2.0.CO;2, 1981.
- Brandes, E. A., and Ziegler, C. L.: Mesoscale downdraft influences on vertical vorticity in a mature mesoscale convective system, *Mon. Wea. Rev.*, 121, 1337–1353, [https://doi.org/10.1175/1520-0493\(1993\)121<1337:MDIOVV>2.0.CO;2](https://doi.org/10.1175/1520-0493(1993)121<1337:MDIOVV>2.0.CO;2), 1993.
- Chen, T., Guo, J., Guo, X., Zhang, Y., Xu, H., and Zhang, D.-L.: On the multiscale

Formatted: Font: Italic

Formatted: Font: Italic

Formatted: Font: Italic

594 processes leading to an extreme gust wind event in East China: Insights from
 595 radar wind profiler mesonet observations. *Journal of Geophysical Research:*
 596 *Atmosphere*, 129, <https://doi.org/10.1029/2024JD041484>, 2024.

597 [Dai, C., Wang, Q., Kalogiros, J. A., Lenschow, D. H., Gao, Z., and Zhou, M.:](#)
 598 [Determining boundary-layer height from aircraft measurements, *Bound.-Lay.*](#)
 599 [Meteorol.](#), 152, 277–302, <https://doi.org/10.1007/s10546-014-9929-z>, 2014.

600 Davies-Jones, R.: Useful, formulas for computing divergence, vorticity, and their
 601 errors from three or more stations, *Mon. Wea. Rev.*, 121: 713-725, 1993.

602 [Dodson, D. S. and Small Griswold, J. D.: Turbulent and boundary layer](#)
 603 [characteristics during VOCALS-REx, *Atmos. Chem. Phys.*, 21, 1937–1961,](#)
 604 <https://doi.org/10.5194/acp-21-1937-2021>, 2021.

605 Fankhauser, J. C., Crook, N. A., Tuttle, J., and Coauthors: Initiation of Deep
 606 Convection along Boundary Layer Convergence Lines in a Semitropical
 607 Environment, *Mon. Wea. Rev.*, **123**(2), 291-314, 1995.

608 Guo, J., Liu, B., Gong, W., Shi, L., Zhang, Y., Ma, Y., Zhang, J., Chen, T., Bai, K.,
 609 Stoffelen, A., de Leeuw, G., and Xu, X.: Technical note: First comparison of
 610 wind observations from ESA's satellite mission Aeolus and ground-based radar
 611 wind profiler network of China, *Atmos. Chem. Phys.*, **21**, 2945–2958,
 612 <https://doi.org/10.5194/acp-21-2945-2021>, 2021a.

613 [Guo, J., Zhang, J., Yang, K., Liao, H., Zhang, S., Huang, K., Lv, Y., Shao, J., Yu, T.,](#)
 614 [Tong, B., Li, J., Su, T., Yim, S. H. L., Stoffelen, A., Zhai, P., and Xu, X.:](#)
 615 [Investigation of near-global daytime boundary layer height using high-resolution](#)
 616 [radiosondes: First results and comparison with ERA-5, MERRA-2, JRA-55, and](#)
 617 [NCEP-2 reanalyses, *Atmos. Chem. Phys.*, 21, 17079–17097,](#)
 618 <https://doi.org/10.5194/acp-21-17079-2021>, 2021b.

619 Guo, J., and Guo, X.: A temporally continuous divergence and vorticity dataset in
 620 Beijing derived from the radar wind profiler mesonet during 2023 [Data set],
 621 <https://doi.org/10.5281/zenodo.15297246>, 2024a.

622 Guo, X., Guo, J., Zhang, D-L., and Yun, Y: Vertical divergence profiles as detected

Formatted: Font: Times New Roman, Not Bold

Formatted: Font: Times New Roman

Formatted: Font: Times New Roman

Formatted: Font: Times New Roman, Not Bold, Not Italic

Formatted: Font: Times New Roman

Field Code Changed

Formatted: Hyperlink, Font: Times New Roman

Deleted: <https://doi.org/10.5281/zenodo.15297207>

Deleted: 14176969

by two wind profiler mesonets over East China: implications for nowcasting convective storms, *Q. J. R. Meteorol. Soc.*, 149(754), 1629-1649, doi:10.1002/qj.4474, 2023.

Guo, X., Guo, J., Chen, T., Li, N., Zhang, F., and Sun, Y.: Revisiting the evolution of downhill thunderstorms over Beijing: a new perspective from a radar wind profiler mesonet, *Atmos. Chem. Phys.*, 24, 8067–8083, <https://doi.org/10.5194/acp-24-8067-2024>, 2024b.

Hendricks, E. A., Montgomery, M. T., Davis, C. A.: On the role of "vortical" hot towers in formation of tropical cyclone Diana, *J Atmos Sci*, 61, 1209-1232. [https://doi.org/10.1175/1520-0469\(2004\)061<1209:TROVHT>2.0.CO;2](https://doi.org/10.1175/1520-0469(2004)061<1209:TROVHT>2.0.CO;2), 2004

Hersbach, H., Bell, B., Berrisford, P., and Coauthors: The ERA5 global reanalysis, *Q. J. R. Meteorol. Soc.*, 146(730), 1999–2049, <https://doi.org/10.1002/qj.3803>, 2020.

Holland, J. Z.: Preliminary report on the BOMEX sea-air interaction program, *Bull. Amer. Meteor. Soc.*, 51, 809 – 820, [https://doi.org/10.1175/1520-0477\(1970\)051,0809:PROTBS.2.0.CO;2](https://doi.org/10.1175/1520-0477(1970)051,0809:PROTBS.2.0.CO;2), 1970.

Johnson, R. H., Chen, S., Toth, J. J.: Circulations associated with a mature-to-decay midlatitude mesoscale convective system. Part I: Surface features-heat bursts and mesoscale development, *Mon. Wea. Rev.*, 117(5), 942-959, [https://doi.org/10.1175/1520-0493\(1989\)117<0942:CAWAMT>2.0.CO;2](https://doi.org/10.1175/1520-0493(1989)117<0942:CAWAMT>2.0.CO;2), 1989.

Kalthoff, N., Adler, B., Barthlott, C., and Coauthors: The impact of convergence zones on the initiation of deep convection: A case study from COPS, *Atmos. Res.* 93(4): 680-694, 2009.

Lai, H. W., Davis, C. A., Jou, B. J.-D.: A subtropical oceanic mesoscale convective vortex observed during SoWMEX/TiMREX, *Mon. Wea. Rev.*, 139(8), 2367-2385, <https://doi.org/10.1175/2010MWR3411.1>, 2011.

Lee, J. L., and Browning, G. L.: Analysis of Errors in the Horizontal Divergence Derived from High Temporal Resolution of the Wind, *Mon. Wea. Rev.*, 122(5), 851-863, doi: 10.1175/1520-0493(1994)122.0.CO;2, 1993.

Lenschow, D. H., Krummel, P. B., and Siems, S. T.: Measuring entrainment,

divergence, and vorticity on the mesoscale from aircraft, *J. Atmos. Oceanic Technol.*, 16, 1384 – 1400, [https://doi.org/10.1175/1520-0426\(1999\)016,1384:MEDAVO.2.0.CO;2](https://doi.org/10.1175/1520-0426(1999)016,1384:MEDAVO.2.0.CO;2), 1999.

Lenschow, D. H., Savic-Jovicic, V., and Stevens, B.: Divergence and vorticity from aircraft air motion measurements, *J. Atmos. Oceanic Technol.*, 24, 2062–2072, <https://doi.org/10.1175/2007JTECHA940.1>, 2007.

Liu, B., Ma, Y., Guo, J., and Coauthors: Boundary layer heights as derived from ground-based radar wind profiler in Beijing, *IEEE Transactions on Geoscience and Remote Sensing*, 57, 8095-8104, <https://doi.org/10.1109/TGRS.2019.2918301>, 2019.

Lock, N. A., and Houston, A. L.: Empirical examination of the factors regulating thunderstorm initiation, *Mon. Wea. Rev.*, **142**, 240-258, <https://doi.org/10.1175/MWR-D-13-00082.1>, 2014.

McCaffrey, K., Bianco, L., Johnston, P., and Wilczak, J. M.: A comparison of vertical velocity variance measurements from wind profiling radars and sonic anemometers, *Atmos. Meas. Tech.*, 10, 999–1015, <https://doi.org/10.5194/amt-10-999-2017>, 2017.

Nitta, T., and Esbensen, S.: Heat and moisture budget analyses using BOMEX data, *Mon. Wea. Rev.*, 102, 17-28, [https://doi.org/10.1175/1520-0493\(1974\)102,0017:HAMBAU.2.0.CO;2](https://doi.org/10.1175/1520-0493(1974)102,0017:HAMBAU.2.0.CO;2), 1974.

Purdom, J. F. W.: Some uses of high-resolution GOES imagery in the mesoscale forecasting of convection and its behavior, *Mon. Wea. Rev.*, **104**, 1474–1483, [https://doi.org/10.1175/1520-0493\(1976\)1042.0.CO;2](https://doi.org/10.1175/1520-0493(1976)1042.0.CO;2), 1976.

Qin, R., and Chen, M.: Impact of a front–dryline merger on convection initiation near a mountain ridge in Beijing, *Mon. Wea. Rev.*, 145, 2611-2633, <https://doi.org/10.1175/MWR-D-16-0369.1>, 2017).

Shapiro, A., Potvin, C. K., and Jidong, G.: Use of a vertical vorticity equation in variational dual-Doppler wind analysis, *J. Atmos. Oceanic Technol.*, 26, 2089–

Formatted: Font: Italic

2106, 2009.

Su, T. N., Li, Z. Q., and Zheng, Y. T.: Cloud-Surface Coupling Alters the Morning Transition from Stable to Unstable Boundary Layer, *Geophys. Res. Lett.*, 50, e2022GL102256, <https://doi.org/10.1029/2022gl102256>, 2023.

Taszarek, M., Púciak, T., Hoogewind, K., Allen, J.T., and Coauthors: Comparison of convective parameters derived from ERA5 and MERRA-2 with rawinsonde Data over Europe and North America, *J. Climate*, 34(8), 3211–3237, 2021.

Trier, S. B., Skamarock, W. C., and LeMone, M. A.: Structure and evolution of the 22 February 1993 TOGA Squall Line: Organization Mechanisms Inferred from Numerical Simulation, *J. Atmos. Sci.*, 54(3), 386-407, [https://doi.org/10.1175/1520-0469\(1997\)054<0386:SAEOTF>2.0.CO;2](https://doi.org/10.1175/1520-0469(1997)054<0386:SAEOTF>2.0.CO;2), 1997.

Ulanski, S. L., and Garstang, M.: The role of surface divergence and vorticity in the life cycle of convective rainfall. Part I: Observations and analysis, *J. Atmos. Sci.*, 35, 1047–1062, [https://doi.org/10.1175/1520-0469\(1978\)035<1063:TROSDA>2.0.CO;2](https://doi.org/10.1175/1520-0469(1978)035<1063:TROSDA>2.0.CO;2), 1978.

Wang, W., Kuo, Y. H., and Warner, T. T.: A diabatically driven mesoscale vortex in the lee of the Tibetan Plateau, *Mon. Wea. Rev.*, 121, 2542–2561, 1993.

Wang, L., Wang, G., Gu, Y., Li, H., Ma, L., Guo, J., and Qiao, L.: Application of Wind Profiler Radar Vertical Radial Velocity, *Meteorological Monthly*, 40, 290-296, doi: 10.7519/j.issn.1000-0526.2014.03.004, 2014.

Weckwerth, T. M., and Parsons, D. B.: A review of convection initiation and motivation for IHOP 2002, *Mon. Wea. Rev.*, 134, 5-22, <https://doi.org/10.1175/MWR3067.1>, 2006.

Wilson, J.W., and Schreiber, W.E.: Initiation of convective storms at radar-observed boundary-layer convergence lines, *Mon. Wea. Rev.*, 114, 2516-2536, [https://doi.org/10.1175/1520-0493\(1986\)114<2516:iocsar>2.0.co;2](https://doi.org/10.1175/1520-0493(1986)114<2516:iocsar>2.0.co;2), 1986.

Wilson, J.W., and Roberts, R.D.: Summary of convective storm initiation and evolution during IHOP: Observational and modeling perspective, *Mon. Wea.*

Formatted: Font: Italic

Rev., **134**, 23–47, <https://doi.org/10.1175/MWR3069.1>, 2006.

Weckwerth, T. M., Hanesiak, J., Wilson, J. W., and Coauthors: Nocturnal convection initiation during PECAN 2015, *Bull. Amer. Meteor. Soc.*, **100**, 2223–2239, <https://doi.org/10.1175/BAMS-D-18-0299.1>, 2019.

Wu, J., Guo, J., Yun, Y., and Coauthors: Can ERA5 reanalysis data characterize the pre-storm environment? *Atmospheric Research*, **297**, 107108, <https://doi.org/10.1016/j.atmosres.2023.107108>, 2023.

Yanai, M., and Nitta, T.: Computation of vertical motion and vorticity budget in a Caribbean easterly wave, *J. Meteor. Soc. Japan*, **45**, 444–466, 1967.

Yin, J., Zhang, D.-L., Luo, Y., and Ma, R.: On the extreme rainfall event of 7 May 2017 over the coastal city of Guangzhou. Part I: Impacts of urbanization and orography, *Mon. Wea. Rev.*, **148**, <https://doi.org/10.1175/MWR-D-19-0212.1>, 2020.

Zhang, D. L., and Fritsch, J. M.: Numerical simulation of the Meso- β scale structure and evolution of the 1977 Johnstown flood. Part II: Inertially stable warm-core vortex and the mesoscale convective complex, *J. Atmos. Sci.*, **43**(18):1913–1944, doi: 10.1175/1520-0469(1986)043<1913:NSOTMS>2.0.CO;2, 1986.

Zhang, D.-L., Gao, K., and Parsons, D. B.: Numerical simulation of an intense squall line during 10–11 June 1985 PRE-STORM. Part I: Model verification, *Mon. Wea. Rev.*, **117**, 960–994, [https://doi.org/10.1175/1520-0493\(1989\)117,0960:NSOALS.2.0.CO;2](https://doi.org/10.1175/1520-0493(1989)117,0960:NSOALS.2.0.CO;2), 1989.

733 **Tables**

734 **Table 1.** General characteristics of the CFL-6 radar wind profiler

Parameters	Values
<u>Direction accuracy</u>	<u>≤ 10°</u>
<u>Speed accuracy</u>	<u>1.5 m s⁻¹</u>
<u>Vertical resolution</u>	<u>120 or 240 m</u>
<u>Minimum height</u>	<u>150 m</u>
<u>Maximum height</u>	<u>10110 m</u>
<u>Averaging time</u>	<u>6-60 min</u>
<u>Operating frequency</u>	<u>1360 MHz</u>
<u>Gain</u>	<u>33 dB</u>
<u>Peak power</u>	<u>9.6 kW</u>
<u>Pulse width</u>	<u>0.8 or 1.6 μs</u>

Formatted: Font: 12 pt, Not Bold

Formatted: Font: (Asian) Times New Roman, 12 pt, Not Italic

Formatted: Font: (Asian) Times New Roman, 12 pt, Not Bold, Not Italic

Figures

Figure 1. (a) Locations of the six radar wind profiler (RWP) stations (black dots). The blue line denotes the administrative boundaries at the provincial level. Four black triangles with number denote the regions used to calculate the horizontal divergence and vertical vorticity with the triangle method. (b) The missing rate of horizontal wind speeds at different heights derived from six RWPs. (c) Vertical profile of the correlation coefficient (R) between horizontal wind speeds derived from the RWP and those from the upper-air soundings (RS) at the Beijing Weather Observatory (BWO). (d) Scatterplots of the horizontal wind speeds at the range of 0.51-4.11 km above ground level (AGL) from the RWP versus RS at the BWO. The red and black dashed lines denote the linear regression and 1:1 line respectively.

Deleted: ¶

Deleted: , which are deployed at Huairou (HR; 40.36°N, 116.63°E), Yanqing (YQ; 40.45°N, 115.97°E), Shangdianzi (SDZ; 40.66°N, 117.11°E), Pinggu (PG; 40.17°N, 117.12°E), Haidian (HD; 39.98°N, 116.28°E), and the Beijing Weather Observatory (BWO; 39.79°N, 116.47°E).

Formatted: Font: Not Bold

Deleted: mesonet

Formatted: Font: (Asian) DengXian

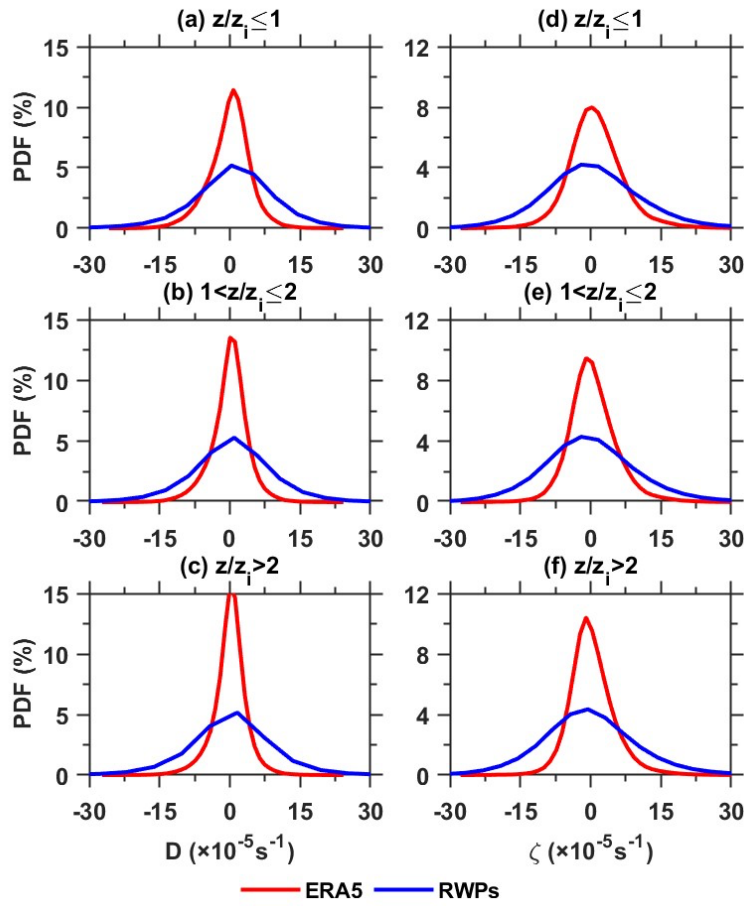
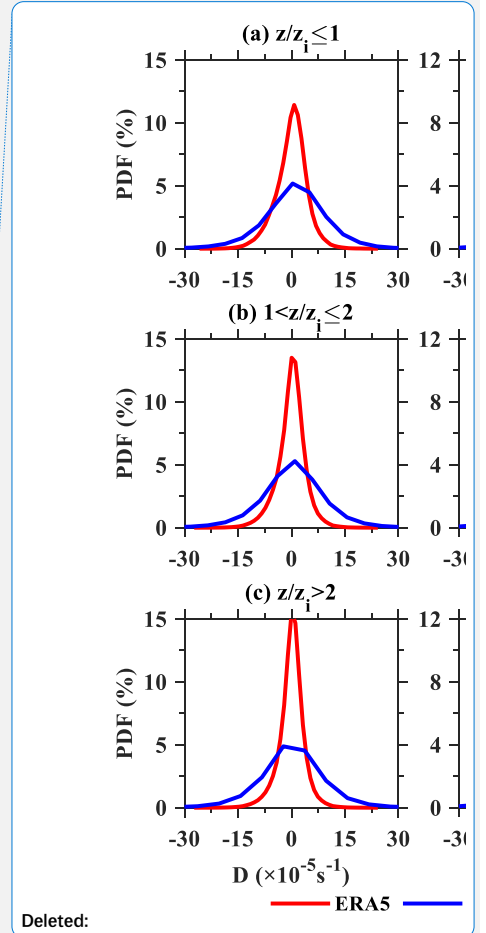


Figure 2. The probability density function (PDF) of horizontal divergence (D) estimated from the measurements of RWPs mesonet (blue line) and ERA5 reanalysis (red line) at the height of (a) $z/z_i \leq 1$, (b) $1 < z/z_i \leq 2$, and (c) $z/z_i > 2$; (d) –(f) the same as (a)–(c) but for the PDF of vertical vorticity (ζ).



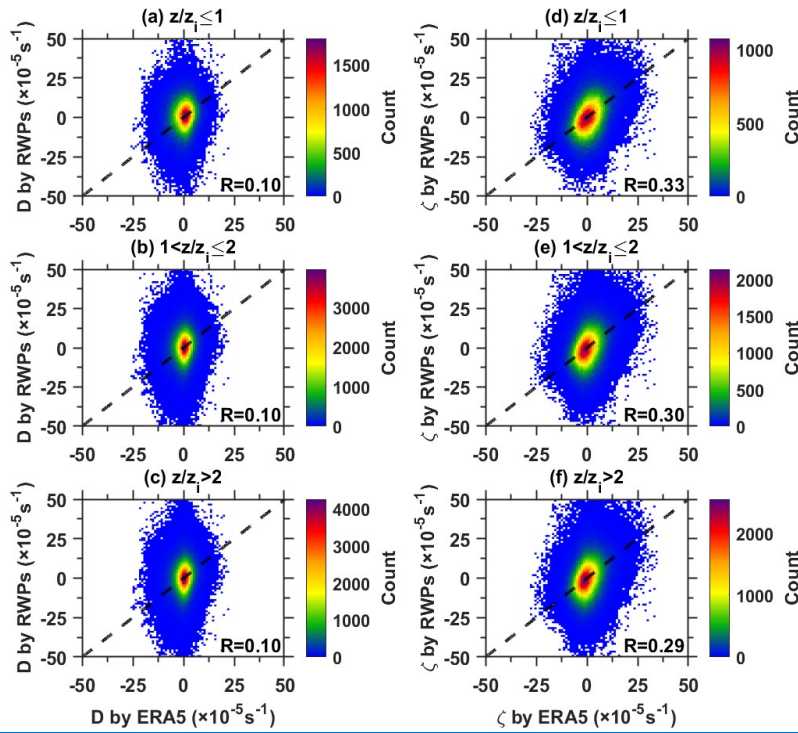
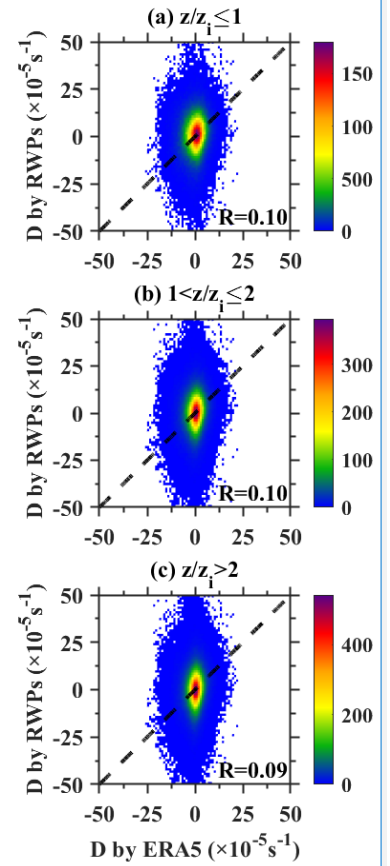


Figure 3. Scatterplots of the horizontal divergence (D) from the measurements of RWP mesonet versus ERA5 reanalysis at the heights of (a) $z/z_i \leq 1$, (b) $1 < z/z_i \leq 2$, and (c) $z/z_i > 2$ with the 1:1 line shown as black-dashed lines, respectively. The color bar indicates the counts of data points. (d)-(f) the same as (a)-(c) but for the vertical vorticity (ζ).



Deleted:

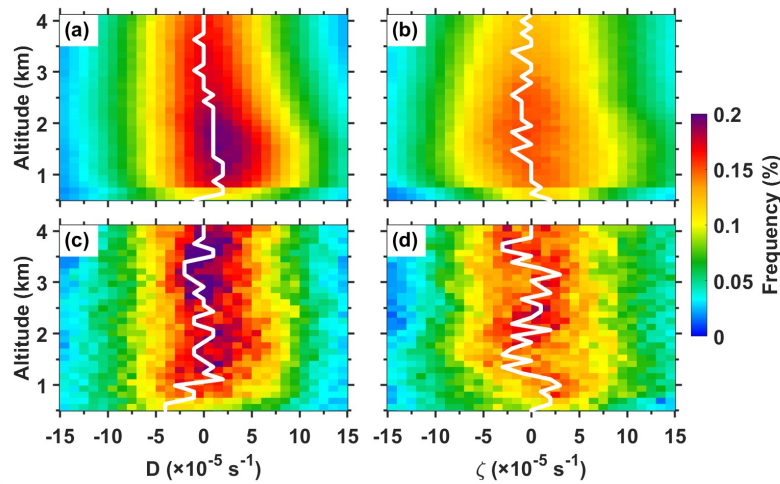


Figure 4. Normalized contoured frequency by altitude (NCFAD) for the horizontal divergence (a) and vertical vorticity (b) between 0.51-4.11 km AMSL as calculated by the RWP mesonet measurements in non-precipitation days of 2023 in Beijing. The white line represents the profile of maximum frequency distribution. (c) and (d) Same as (a) and (b), except for the frequency distribution within 1-hour preceding rainfall events.

Deleted: 95

Deleted: preceding all the rainfall events

Deleted: BMR

Deleted: Note that t

Deleted: Gray layer is not analyzed due to the error of wind measurements....

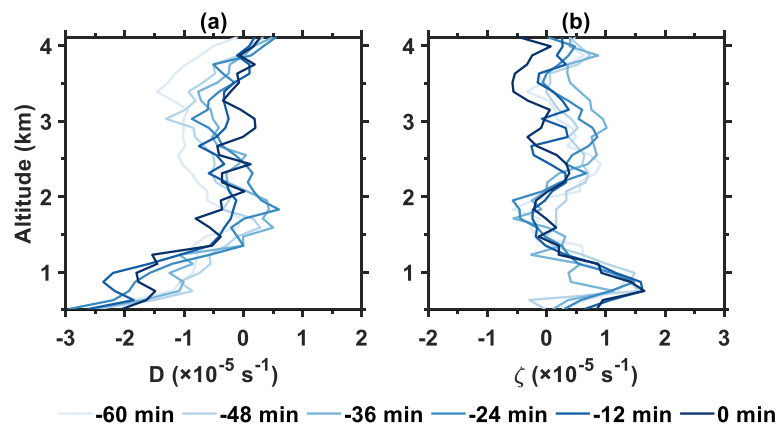


Figure 5. Evolution of the profiles of horizontal divergence (a) and vertical vorticity (b) between 0.51–4.11 km AMSL averaged over 12 minutes, which are calculated from the RWP mesonet (blue line) in Beijing within 1-hour before the onset of rainfall events in 2023.

Deleted: 95

Deleted: the BMR

Deleted: The lowest atmospheric layer shaded in grey is not analyzed due to the error of wind measurements from

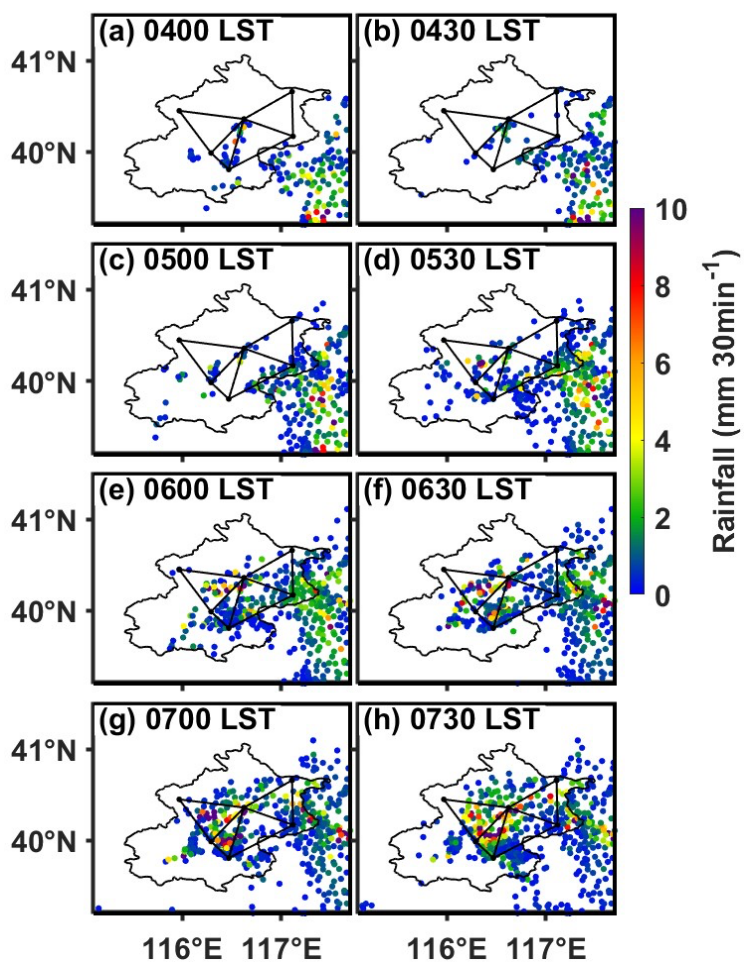


Figure 6. Accumulated precipitation ($\text{mm } 30\text{min}^{-1}$; colored dots) at (a) 0400 (b) 0430, (c) 0500, (d) 0530, (e) 0600, (f) 0630, (g) 0700 and (h) 0730 LST 22 July, 2023. The RWP mesonet is also plotted (see Figure 1a for the location).

Formatted: Superscript

Formatted: Font: (Asian) DengXian

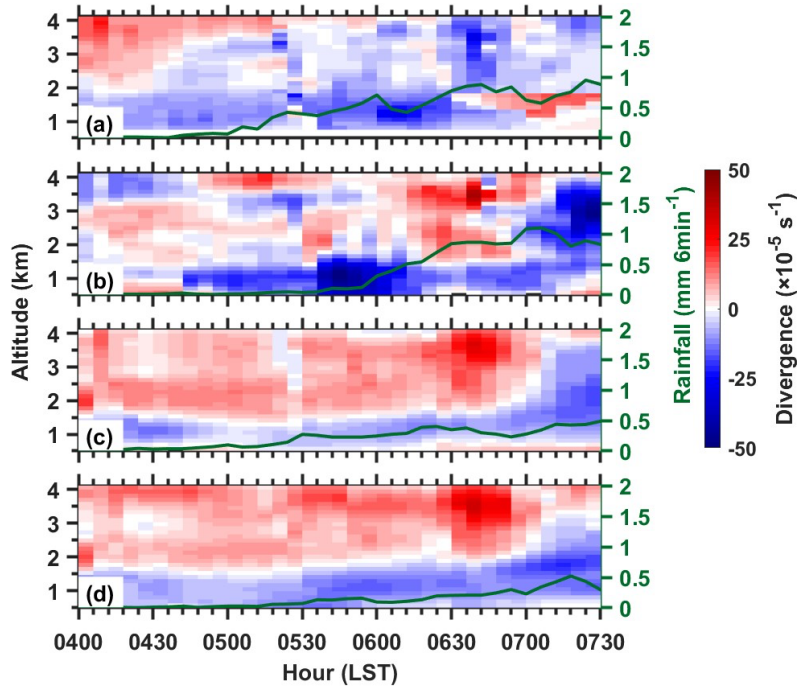


Figure 7. The vertical profiles of the triangle-averaged divergence (10^{-5} s^{-1} , shading) derived from the RWP mesonet in Beijing at 120 m vertical resolution between 0.51 and 4.11 km AMSL at 6-min intervals during the period of 0400–0730 LST 22 July, 2023 for (a) triangle 1, (b) triangle 2, (c) triangle 3, and (d) triangle 4 (see their distributions in Figure 1a). Green-dotted lines represent the triangle-area-averaged rainfall amount ($\text{mm } 6\text{min}^{-1}$).